Magnetic charges and magnetoelectricity in hexagonal rare-earth manganites and ferrites

Meng Ye* and David Vanderbilt
Department of Physics & Astronomy, Rutgers University, Piscataway, New Jersey 08854, USA

(Dated: April 15, 2015)

Magnetoelectric (ME) materials are of fundamental interest and show broad potential for technological applications. Commonly the dominant contribution to the ME response is the lattice-mediated one, which is proportional to both the Born electric charge Z^{e} and its analogue, the dynamical magnetic charge Z^{m}. Our previous study has shown that exchange striction acting on noncollinear spins induces much larger magnetic charges than those that depend on spin-orbit coupling. The hexagonal manganites RMnO$_3$ and ferrites RFeO$_3$ (R = Sc, Y, In, Ho-Lu) exhibit strong couplings between electric, magnetic and structural degrees of freedom, with the transition-metal ions in the basal plane antiferromagnetically coupled through super-exchange so as to form a 120° noncollinear spin arrangement. Here we present a theoretical study of the magnetic charges, and of the spin-lattice and spin-electronic ME constants, in these hexagonal manganites and ferrites, clarifying the conditions under which exchange striction leads to an enhanced Z^{m} values and anomalously large in-plane spin-lattice ME effects.

PACS numbers: 75.85.+t,75.30.Et, 75.70.Tj, 75.47.Lx

I. INTRODUCTION

The cross-coupling between magnetic, electric, and elastic properties can lead to a plethora of novel and profound physical phenomena, with potentially broad and innovative applications. Magnetoelectric (ME) effects are those in which the electric polarization $\mathbf{P}$ responds to an applied magnetic field $\mathbf{H}$, or magnetization $\mathbf{M}$ responds to an applied electric field $\boldsymbol{\mathcal{E}}$. The ME coupling (MEC) between magnetic and electric properties has motivated intense experimental and theoretical investigations in bulk single crystals, thin films, composite layers, and organic-inorganic hybrid materials in recent years.[1–11]

At the linear-response level, the linear MEC tensor α is defined as

$$\alpha_{\beta\nu} = \frac{\partial P_\beta}{\partial H_\nu}\Big|_{\boldsymbol{\mathcal{E}}} = \mu_0 \frac{\partial M_\nu}{\partial \mathcal{E}_\beta}\Big|_{\mathbf{H}}, \tag{1}$$

where indices β and ν denote the Cartesian directions and μ_0 is the vacuum permeability. From a theoretical point of view, the linear ME effect can be decomposed into electronic (frozen-ion), ionic (lattice-mediated), and strain-mediated responses.[11] Each term can be further subdivided into spin and orbital contributions based on the origin of the induced magnetization. As the orbital moment is usually strongly quenched on the transition-metal sites, most phenomenological and first-principles studies have focused on the spin-electronic[12] and the spin-lattice[13–15] contributions. The lattice response can be written, following Ref. 13, as

$$\alpha^{\mathrm{latt}}_{\beta\nu} = \Omega_0^{-1}\mu_0 Z^{\mathrm{e}}_{m\beta}\,(K^{-1})_{mn}\,Z^{\mathrm{m}}_{n\nu}, \tag{2}$$

(sum over repeated indices implied), i.e., as a matrix product of the dynamical Born electric charge Z^{e}, the inverse force-constant matrix K^{-1}, and the dynamical magnetic charge Z^{m}, where m and n are composite labels for an atom and its displacement direction. Ω_0 is the unit cell volume. Note that Z^{m} is the magnetic analog of the dynamical Born charge, and is defined as

$$Z^{\mathrm{m}}_{m\nu} = \Omega_0 \frac{\partial M_\nu}{\partial u_m}\Big|_{\boldsymbol{\mathcal{E}},\mathbf{H},\eta} = \mu_0^{-1} \frac{\partial F_m}{\partial H_\nu}\Big|_{\boldsymbol{\mathcal{E}},\mathbf{u},\eta}, \tag{3}$$

where u_m is an internal displacement, F_m is an atomic force, and η is a homogeneous strain. In principle, Z^{m} has both spin and orbital parts, corresponding respectively to spin and orbital contributions to M_ν, or Zeeman and $\mathbf{p}\cdot\mathbf{A}$ terms induced by H_ν, but we shall focus on the spin part in the following. Our previous first-principles study has shown that exchange striction acting on noncollinear spin structures induces much larger magnetic charges than when Z^{m} is driven only by spin-orbit coupling (SOC). Therefore, exchange striction provides a promising mechanism for obtaining large MECs.[16]

The hexagonal manganites RMnO$_3$ and ferrites RFeO$_3$ (R = Sc, Y, In, and Ho-Lu) form an interesting class of materials exhibiting strong couplings between electric, magnetic, and structural degrees of freedom.[17] A series of first-principles[15,18–20] and phenomenological[21] studies have greatly enhanced our understanding of the coupled properties. The ferroelectricity is induced by the structural trimerization, and the direction of the spontaneous polarization is related to the trimerization pattern.[19] An interesting "cloverleaf" pattern formed from interlocking domain walls between structural and ferroelectric domains has been found in hexagonal RMnO$_3$ and is now understood in terms of Landau theory.[21–23] Hexagonal RMnO$_3$ and RFeO$_3$ have rich magnetic phase diagrams and show considerable potential for manipulation and practical applications.[24–26] The magnetic order has two different origins, with the transition-metal Mn^{3+} or Fe^{3+} sublattices ordering first, often followed by ordering of the rare-earth ions R^{3+} at lower temperature. The magnetic anisotropy is easy-plane and easy-axis for $3d$ and $4f$ spins respectively; the $3d$ moments are antiferromagnetically coupled through superexchange so as to form a 120° noncollinear arrangement in the x-y plane, while the $4f$ rare-earth moments are collinear along the hexagonal z axis.

The low-temperature magnetic phases of $R\mathrm{MnO}_3$ and $R\mathrm{FeO}_3$ allow a linear ME effect to be present. The recently developed ME force microscopy technique has been used successfully to observe the ME domains in ErMnO_3.[27] In that work, a large ME component $\alpha_{zz} \sim 13$ ps/m has been measured at 4 K, which is below the Mn^{3+} ordering temperature of 81 K but above the Er^{3+} ordering temperature of 2 K. However, first-principles calculations predict that the SOC-induced spin-lattice α_{zz} arising from the Mn^{3+} order is 0.7-1.0 ps/m.[15] This discrepancy suggests that the dominant ME effect in the hexagonal $\hat{z}$ direction is mediated by the Er^{3+} $4f$ electrons in ErMnO_3. The in-plane ME effect, which has not been measured or calculated, has a different origin. It is dominated by an exchange-striction mechanism on the Mn^{3+} sublattice, because the noncollinear spin pattern is sensitive to the lattice distortion. Thus, hexagonal $R\mathrm{MnO}_3$ and $R\mathrm{FeO}_3$ are good candidates to show exchange-striction enhanced magnetic charges and anomalously large spin-lattice MECs.

In this work, we use first-principles density-functional methods to study the magnetic charges and the spin-induced MECs arising from the $3d$ electrons in hexagonal HoMnO_3, ErMnO_3, YbMnO_3, LuMnO_3, and LuFeO_3. For the transverse magnetic charge components and MECs, we also provide a comparison between results induced solely by exchange striction and ones including SOC. Our results confirm that the exchange striction greatly enhances the in-plane magnetic charges, while the SOC contribution is minor for most components except on Mn atoms. However, the effect of SOC on the MECs is surprisingly large in many cases. This occurs because the exchange-striction contribution tends to be reduced by cancellations between modes, while the SOC contribution is mainly associated with a few low-frequency modes. The in-plane ME responses are discussed case by case, and the conditions under which exchange striction leads to anomalously large in-plane spin-lattice MECs are clarified.

The paper is organized as follows. In Sec. II A and II B we introduce the geometric structure and magnetic order of hexagonal $R\mathrm{MnO}_3$ and $R\mathrm{FeO}_3$. In Sec. II C we analyze the tensor symmetries of the Born charges, magnetic charges and MECs in two different magnetic phases of $R\mathrm{MnO}_3$ and $R\mathrm{FeO}_3$. The computational details are described in Sec. II D. The results and discussion of Born charges, magnetic charges and MECs in $R\mathrm{MnO}_3$ and LuFeO_3 are presented in Sec. III. We summarize and give our conclusions in Sec.IV.

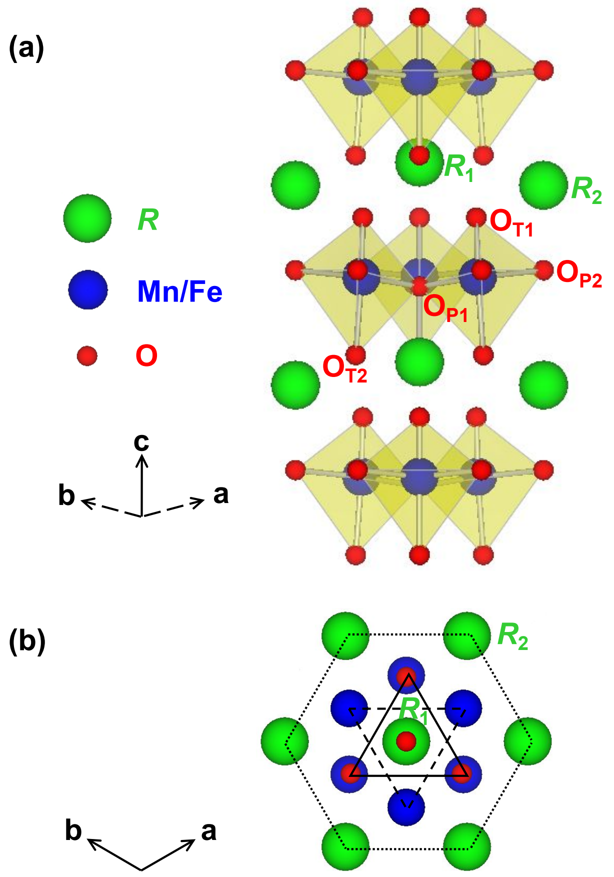

FIG. 1. Structure of ferroelectric hexagonal $R\mathrm{MnO}_3$ (6 f.u. per primitive cell). (a) Side view from [110]. (b) Plan view from [001]; dashed (solid) triangle indicates three Mn^{3+} connected via $\mathrm{O_{P1}}$ to form a triangular sublattice at $z = 0$ $(z = 1/2)$.

II. PRELIMINARIES

A. Hexagonal $R\mathrm{MnO}_3$

Above the structural transition temperature $T_c \sim 900$-1500 K, the hexagonal manganites $R\mathrm{MnO}_3$ (R = Sc, Y, In, and Ho-Lu) are paraelectric insulators. The space group is P6_3/mmc with two formula units (f.u.) per primitive cell. Below T_c, the size mismatch between the small-radius R^{3+} ion and the large MnO_5 bipyramid leads to an inward tilting of the three corner-shared MnO_5 polyhedra and an associated "one-up/two-down" buckling of the R^{3+} ion layer, as shown in Fig. 1. The transition triples ("trimerizes") the unit cell, lowers the structural symmetry to P6_3cm, and induces ferroelectricity. As the induced polarization is nonlinearly coupled to the trimerization, these systems are improper ferroelectrics.[18,19,21]

The Mn^{3+} magnetic order develops below the Néel temperature T_N of ~ 70 - 130 K. The in-plane Mn-O-Mn

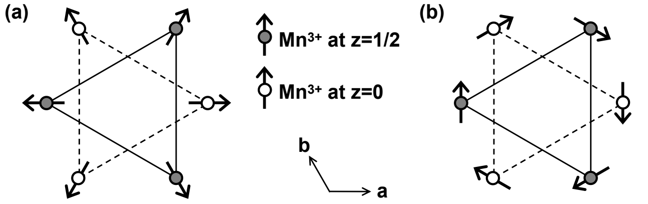

FIG. 2. Magnetic phases of hexagonal RMnO$_3$ and RFeO$_3$. Mn^{3+} ions form triangular sublattices at $z = 0$ (dash line) and $z = 1/2$ (solid line). (a) A$_2$ phase with magnetic symmetry P6$_3$c$'$m$'$; spins on a given Mn^{3+} layer point all in or all out. (b) A$_1$ phase with the magnetic symmetry P6$_3$cm, with Mn^{3+} spins pointing tangentially to form a vortex pattern. The A$_1$ and A$_2$ phases differ by a 90° global rotation of the spins. The B$_1$ and B$_2$ phases can be obtained from A$_2$ and A$_1$ by reversing the spins on the dashed triangles.

superexchange determines the noncollinear 120° antiferromagnetic (AFM) order on the Mn^{3+} triangular lattice. On the other hand, the inter-plane Mn-O-R-O-Mn exchange, which is two orders of magnitude weaker than the in-plane exchange, modulates the relative spin directions between two consecutive Mn planes.[15,24] At temperatures lower than $\sim 5.5\,$K, the rare-earth ions with partially filled $4f$ shells develop collinear spin order along the hexagonal z direction. For the Mn^{3+} order, there are four distinct magnetic phases, namely A$_1$ (P6$_3$cm), A$_2$ (P6$_3$c$'$m$'$), B$_1$ (P6$_3'$cm$'$), and B$_2$ (P6$_3'$c$'$m). The linear ME effect exists only in A$_1$ and A$_2$ phases. The A$_1$ and A$_2$ phases are shown in Fig. 2; the B$_1$ and B$_2$ phases can be obtained from A$_2$ and A$_1$ by reversing the spins on the dashed triangles. From previous experiments, it is known that at zero temperature without a magnetic field, HoMnO$_3$ is in the A$_1$ phase, while ErMnO$_3$, YbMnO$_3$, and LuMnO$_3$ are not in either A phase. Under a weak magnetic field along the $\hat{z}$ direction, ErMnO$_3$ and YbMnO$_3$ undergo a transition into the A$_2$ phase.[24–26]

B. Hexagonal RFeO$_3$

Epitaxially grown thin-film hexagonal RFeO$_3$ has a similar structure as hexagonal RMnO$_3$, with improper ferroelectricity below $\sim 1000\,$K. Replacing Mn^{3+} with Fe^{3+} introduces larger spin moments and stronger superexchange interactions in the basal plane. In a recent experiment, AFM order has been found to develop at $T_{\rm N} = 440\,$K followed by a spin-reorientation transition below $T_{\rm R} = 130\,$K in LuFeO$_3$.[28] It has also been confirmed that below 5 K, the magnetic structure of LuFeO$_3$ is that of the A$_2$ phase.[29]

C. Symmetry

Our purpose is to understand the mechanisms that generate large magnetic charges that may in turn induce anomalously large spin-lattice MECs. Therefore, we focus on the A$_1$ and A$_2$ magnetic phases, shown in Fig. 2, which allow a linear MEC to exist. ErMnO$_3$, YbMnO$_3$, and LuMnO$_3$ actually adopt other phases as their ground-state magnetic order at low temperature. Nevertheless, we include them for purposes of comparison when calculating the properties of the hexagonal RMnO$_3$ materials in the A$_2$ phase. We also study LuFeO$_3$ in the A$_2$ phase, and for HoMnO$_3$ we study both the A$_1$ and A$_2$ phases.

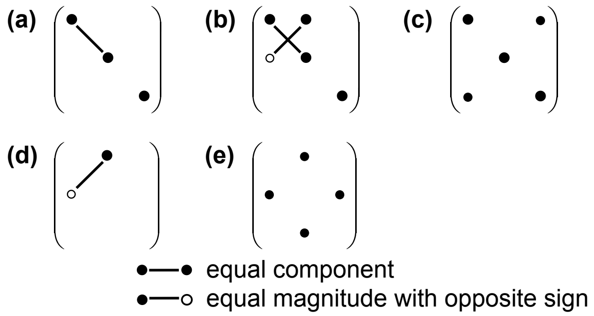

FIG. 3. Symmetry patterns of Born charges, magnetic charges and ME tensors in RMnO$_3$ and RFeO$_3$. (a) Tensor form of the ME coupling in the A$_2$ phase, Born charges on R_1 and O$_{\rm P1}$ sites in either A phase, and magnetic charges on the same sites in the A$_2$ phase. (b) Tensor form of the Born and magnetic charges on R_2 and O$_{\rm P2}$ sites in either A phase. (c) Tensor form of the Born charges on Mn, Fe, O$_{\rm T1}$, and O$_{\rm T2}$ sites lying on an M_y mirror plane in either A phase, and of the magnetic charges on the same sites in the A$_2$ phase. (d) Tensor form of the ME coupling in the A$_1$ phase, and of the magnetic charges on R$_1$ and O$_{\rm P1}$ sites in the A$_1$ phase. (e) Tensor form of the magnetic charges on Mn, Fe, O$_{\rm T1}$, and O$_{\rm T2}$ sites lying on an M_y mirror plane in the A$_1$ phase.

The A$_1$ and A$_2$ phases have the same P6$_3$cm structural symmetry, so the forms of the atomic Born charge tensors in the two phases are the same. The Born charges for R_1 and O$_{\rm P1}$ take the tensor form shown in Fig. 3(a), while those of R_2 and O$_{\rm P2}$ have the symmetry pattern shown in Fig. 3(b). For the Mn, Fe, O$_{\rm T1}$, and O$_{\rm T2}$ sites lying on a vertical M_y mirror plane, the Born charges are as given in Fig. 3(c); for the partner sites related by rotational symmetry, the tensors also need to be rotated accordingly.

The symmetry forms of the atomic magnetic charge tensors can be derived from the on-site magnetic point symmetries. For the A$_1$ phase, the magnetic space group is P6$_3$cm and the magnetic charges of R_1 and O$_{\rm P1}$ take the forms given in Fig. 3(d); those for R_2 and O$_{\rm P2}$ have the tensor symmetry shown in Fig. 3(b); and for Mn, Fe, O$_{\rm T1}$, and O$_{\rm T2}$ they can be written in the form of Fig. 3(e). For the A$_2$ phase, the magnetic group is P6$_3$c$'$m$'$; all the improper operators are associated with the time-reversal operation, so the magnetic charges have the same tensor forms as the Born charges.

A symmetry analysis of the structure and the mag-

TABLE I. Atomic Born charge tensors Z^{e} (in units of $|e|$) for $\mathrm{LuMnO_3}$ and $\mathrm{LuFeO_3}$ in the $\mathrm{A_2}$ phase. TM = Mn or Fe.

	$\mathrm{LuMnO_3}$	$\mathrm{LuFeO_3}$		$\mathrm{LuMnO_3}$	$\mathrm{LuFeO_3}$
$Z^{\mathrm{e}}_{xx}(\mathrm{Lu_1})$	3.61	3.79	$Z^{\mathrm{e}}_{xz}(\mathrm{O_{T1}})$	0.19	0.11
$Z^{\mathrm{e}}_{zz}(\mathrm{Lu_1})$	4.12	3.94	$Z^{\mathrm{e}}_{zz}(\mathrm{O_{T1}})$	−3.19	−3.21
$Z^{\mathrm{e}}_{xx}(\mathrm{Lu_2})$	3.66	3.84	$Z^{\mathrm{e}}_{xx}(\mathrm{O_{T2}})$	−1.90	−2.15
$Z^{\mathrm{e}}_{yx}(\mathrm{Lu_2})$	0.13	0.15	$Z^{\mathrm{e}}_{zx}(\mathrm{O_{T2}})$	−0.20	−0.19
$Z^{\mathrm{e}}_{zz}(\mathrm{Lu_2})$	3.96	3.88	$Z^{\mathrm{e}}_{yy}(\mathrm{O_{T2}})$	−1.85	−2.13
$Z^{\mathrm{e}}_{xx}(\mathrm{TM})$	3.17	2.96	$Z^{\mathrm{e}}_{xz}(\mathrm{O_{T2}})$	−0.18	−0.11
$Z^{\mathrm{e}}_{zx}(\mathrm{TM})$	0.44	0.21	$Z^{\mathrm{e}}_{zz}(\mathrm{O_{T2}})$	−3.33	−3.30
$Z^{\mathrm{e}}_{yy}(\mathrm{TM})$	3.26	3.01	$Z^{\mathrm{e}}_{xx}(\mathrm{O_{P1}})$	−3.00	−2.40
$Z^{\mathrm{e}}_{xz}(\mathrm{TM})$	0.07	−0.02	$Z^{\mathrm{e}}_{zz}(\mathrm{O_{P1}})$	−1.54	−1.61
$Z^{\mathrm{e}}_{zz}(\mathrm{TM})$	3.95	4.16	$Z^{\mathrm{e}}_{xx}(\mathrm{O_{P2}})$	−3.05	−2.45
$Z^{\mathrm{e}}_{xx}(\mathrm{O_{T1}})$	−1.92	−2.19	$Z^{\mathrm{e}}_{yx}(\mathrm{O_{P2}})$	−0.03	−0.02
$Z^{\mathrm{e}}_{zx}(\mathrm{O_{T1}})$	0.25	0.25	$Z^{\mathrm{e}}_{zz}(\mathrm{O_{P2}})$	−1.43	−1.52
$Z^{\mathrm{e}}_{yy}(\mathrm{O_{T1}})$	−2.00	−2.28			

TABLE II. Eigenvalues of the force-constants matrix (eV/Å^2) for IR-active modes in $\mathrm{LuMnO_3}$ and $\mathrm{LuFeO_3}$ in the $\mathrm{A_2}$ phase, excluding translational modes.

A_1 modes		E_1 modes	
$\mathrm{LuMnO_3}$	$\mathrm{LuFeO_3}$	$\mathrm{LuMnO_3}$	$\mathrm{LuFeO_3}$
4.24	3.48	3.32	3.56
7.44	6.70	4.68	4.62
8.74	8.41	6.73	6.97
11.51	11.47	7.35	8.09
14.01	12.03	8.63	8.83
15.60	15.59	9.56	9.24
22.66	20.53	11.36	11.37
25.87	22.83	12.46	12.46
35.82	28.46	13.02	13.85
		14.09	14.92
		16.49	16.87
		17.37	17.35
		23.36	21.19
		37.75	28.75

netic space group identifies the phonon modes that couple to the electromagnetic field. The infrared (IR)-active phonon modes that couple to the electric field are the longitudinal A_1 modes and the transverse E_1 modes,

$$\Gamma_{\mathrm{IR}} = 10A_1 + 15E_1\,, \tag{4}$$

including the three acoustic modes. The magnetization is generated by phonon modes that couple to the magnetic field. In the $\mathrm{A_1}$ phase, the magneto-active phonon modes are the longitudinal A_2 modes and the transverse E_1 modes,

$$\Gamma^{\mathrm{A_1}}_{\mathrm{mag}} = 5A_2 + 15E_1\,, \tag{5}$$

where one pair of acoustic E_1 modes are included. In the $\mathrm{A_2}$ phase, on the other hand, the IR- and magneto-active phonon modes are identical, since the magnetic and Born charge tensors have the same form in this case.

For the MECs in the $\mathrm{A_1}$ phase, as the longitudinal IR-active and magneto-active modes are mutually exclusive, the ME tensor takes the form of Fig. 3(d), which does not have a longitudinal ME component. For the $\mathrm{A_2}$ magnetic phase, the A_1 and E_1 modes are both IR-active and magneto-active, so that the ME tensor has both longitudinal and transverse components and adopts the form shown in Fig. 3(a).

D. First-principles methods

Our calculations are performed with plane-wave density functional theory (DFT) implemented in VASP[30] using the generalized-gradient approximation parametrized by the Perdew-Burke-Ernzerhof functional.[31] The ionic core environment is simulated by projector augmented wave (PAW) pseudopotentials,[32] and the $4f$ electrons are placed in the PAW core. We use a Hubbard $U = 4.5\,\mathrm{eV}$ and $J = 0.95\,\mathrm{eV}$ on the d orbitals of the Mn/Fe atoms, and the moment on the rare-earth ions are not considered.[15] The structures are fully relaxed in the DFT+U[33] calculations with their non-collinear spin arrangements in two cases, when SOC is present and when it is absent. In our noncollinear magnetization calculation, a high cutoff energy 700 eV and a tight energy error threshold 1.0×10^{-9} eV are necessary to get fully converged magnetic properties. The Born effective charge tensors and the Γ-point force-constant matrices are obtained using linear-response methods in the absence of SOC. The dynamical magnetic charges are computed by applying a uniform Zeeman field[12] to the crystal and computing the resulting forces. Polarization is calculated using the Berry phase formalism.[34] A $4\times4\times2$ Γ-centered k-point mesh is used in the calculations.

III. RESULTS AND DISCUSSION

A. Born charge and force-constant matrix

The f electrons are not included in our calculations for the hexagonal $R\mathrm{MnO_3}$ class of materials, so the major differences between compounds result from the variation of the rare-earth radius; the trimerization tends to increase as the radius of the rare-earth element decreases. Because of the similarity in the geometric structures, the dielectric and phonon properties are almost identical in the $R\mathrm{MnO_3}$ compounds, regardless of the magnetic ordering. In Tables I and II we list the Born charge tensors and the eigenvalues of the force-constant matrix for the IR-active modes of $\mathrm{LuMnO_3}$ and $\mathrm{LuFeO_3}$. Only small differences are observed between $\mathrm{LuMnO_3}$ and $\mathrm{LuFeO_3}$, reflecting the different transition-metal atom. The results for the other $R\mathrm{MnO_3}$ compounds are quite similar to those of $\mathrm{LuMnO_3}$ and are given for completeness in the Supplement.

TABLE III. Longitudinal magnetic charge components Z^{m} ($10^{-3}\mu_{\mathrm{B}}/\mathrm{\AA}$) of $R\mathrm{MnO_3}$ and $\mathrm{LuFeO_3}$ in the $\mathrm{A_2}$ phase. All components vanish in the absence of SOC.

	$\mathrm{HoMnO_3}$	$\mathrm{ErMnO_3}$	$\mathrm{YbMnO_3}$	$\mathrm{LuMnO_3}$	$\mathrm{LuFeO_3}$
$Z^{\mathrm{m}}_{zz}(R_1)$	−50	−53	−53	−67	7
$Z^{\mathrm{m}}_{zz}(R_2)$	14	35	24	16	7
$Z^{\mathrm{m}}_{xz}(\mathrm{TM})$	−92	−86	−61	−67	9
$Z^{\mathrm{m}}_{zz}(\mathrm{TM})$	24	1	6	25	2
$Z^{\mathrm{m}}_{xz}(\mathrm{O_{T1}})$	−49	−44	−41	−19	23
$Z^{\mathrm{m}}_{zz}(\mathrm{O_{T1}})$	99	81	53	33	22
$Z^{\mathrm{m}}_{xz}(\mathrm{O_{T2}})$	−7	−12	−12	−12	0
$Z^{\mathrm{m}}_{zz}(\mathrm{O_{T2}})$	−119	−94	−64	−49	−25
$Z^{\mathrm{m}}_{zz}(\mathrm{O_{P1}})$	−276	−257	−230	−190	54
$Z^{\mathrm{m}}_{zz}(\mathrm{O_{P2}})$	141	140	125	100	−35

TABLE IV. Transverse magnetic charge components Z^{m} ($10^{-2}\mu_{\mathrm{B}}/\mathrm{\AA}$) of $\mathrm{HoMnO_3}$ in the $\mathrm{A_1}$ phase, as computed inculding or excluding SOC.

	Total	No SOC		Total	No SOC
$Z^{\mathrm{m}}_{yx}(\mathrm{Ho_1})$	−25	−28	$Z^{\mathrm{m}}_{zy}(\mathrm{O_{T1}})$	−188	−230
$Z^{\mathrm{m}}_{xx}(\mathrm{Ho_2})$	−15	−18	$Z^{\mathrm{m}}_{yx}(\mathrm{O_{T2}})$	−57	−67
$Z^{\mathrm{m}}_{yx}(\mathrm{Ho_2})$	−1	3	$Z^{\mathrm{m}}_{xy}(\mathrm{O_{T2}})$	−20	−26
$Z^{\mathrm{m}}_{yx}(\mathrm{Mn})$	92	54	$Z^{\mathrm{m}}_{zy}(\mathrm{O_{T2}})$	−192	−231
$Z^{\mathrm{m}}_{xy}(\mathrm{Mn})$	−10	2	$Z^{\mathrm{m}}_{yx}(\mathrm{O_{P1}})$	−483	−551
$Z^{\mathrm{m}}_{zy}(\mathrm{Mn})$	41	48	$Z^{\mathrm{m}}_{xx}(\mathrm{O_{P2}})$	395	461
$Z^{\mathrm{m}}_{yx}(\mathrm{O_{T1}})$	23	28	$Z^{\mathrm{m}}_{yx}(\mathrm{O_{P2}})$	184	253
$Z^{\mathrm{m}}_{xy}(\mathrm{O_{T1}})$	−7	−7			

B. Magnetization and magnetic charge

In the $\mathrm{A_2}$ phase, the trimerization induces not only an electric polarization, but also a weak ferromagnetism in the $\hat{z}$ direction arising from out-of-plane tilting of the $\mathrm{Mn^{3+}}$ spin moments induced by SOC. The net magnetizations in the 30-atom unit cell for $\mathrm{A_2}$-phase $\mathrm{HoMnO_3}$, $\mathrm{ErMnO_3}$, $\mathrm{YbMnO_3}$, and $\mathrm{LuMnO_3}$ are 0.309, 0.303, 0.292, and $0.268\,\mu_B$, respectively. These magnetic moments are found to depend almost linearly on the tilting angle of the $\mathrm{MnO_5}$ bipyramids, which takes values of 5.03°, 5.07°, 5.16°, and 5.21° respectively in these four compounds, but in any case the variation is not very large. In contrast, the result for $\mathrm{LuFeO_3}$ is $-0.077\,\mu_B$, which is much smaller and of opposite sign compared with the $R\mathrm{MnO_3}$ materials.

The magnetic charges defined in Eq. (3) are more sensitive to the local environment, and now the differences between $R\mathrm{MnO_3}$ compounds are more significant. We divide the magnetic charge components into two groups that we label as "longitudinal" and "transverse" depending on whether the coupling is to magnetic fields along the $\hat{z}$ direction or in the x-y plane respectively.[?]

The longitudinal magnetic charge components are calculated with a magnetic field directed along $\hat{z}$, which is roughly perpendicular to the spin directions. These components are only non-zero when SOC is considered. The scenario here is similar to the case of a transverse magnetic field (H_x or H_y) applied to $\mathrm{Cr_2O_3}$, since the magnetization is along the z axis for $\mathrm{Cr_2O_3}$. It is therefore not surprising to find that the longitudinal magnetic charges of $R\mathrm{MnO_3}$ and $\mathrm{LuFeO_3}$ in Table III are comparable to the SOC-induced transverse magnetic charges in $\mathrm{Cr_2O_3}$.[16] The longitudinal magnetic charges for $\mathrm{O_{P1}}$ and $\mathrm{O_{P2}}$ in $\mathrm{LuFeO_3}$ are opposite to, and about three times smaller than, the ones in $R\mathrm{MnO_3}$. These results explain the differences between $R\mathrm{MnO_3}$ and $\mathrm{LuFeO_3}$ regarding the magnitude and the direction of the weak ferromagnetism, which is generated by trimerization distortions involving vertical displacements of $\mathrm{O_{P1}}$ and $\mathrm{O_{P2}}$.

For the response to transverse magnetic fields, both the field and the spins lie in the basal plane, so the dynamical magnetic charges are driven by both SOC and exchange striction. As the exchange-striction strength can exceed that of the SOC by orders of magnitude in some materials, it is worthwhile to understand the relative size of these two effects in $R\mathrm{MnO_3}$ and $\mathrm{LuFeO_3}$. In Tables IV and V we present the transverse magnetic charges induced with and without SOC in the $\mathrm{A_1}$ and $\mathrm{A_2}$ phases. It is obvious that the SOC contributions are an order of magnitude smaller for many transverse components. Similarly, the magnetic charges induced by exchange striction are about ten times larger than the SOC-driven longitudinal ones in Table III. However, the SOC is crucial for the Mn atoms and it even reverses the signs of their transverse magnetic charges.

C. Magnetoelectric effect

We calculate the spin-lattice MEC from Eq. (2) using our computed Born charges, force-constant matrices, and magnetic charges. The spin-electronic contributions are calculated based on the $\partial P/\partial H$ version of Eq. (1) with the lattice degrees of freedom frozen. We further subdivide the ME tensor components into longitudinal and transverse ones based on the direction of $\mathbf{H}$ relative to the hexagonal axis as before, so that the longitudinal (transverse) spin-lattice MEC is calculated using the longitudinal (transverse) magnetic charge components. The MEC tensor elements allowed by symmetry are the longitudinal α_{zz} and transverse $\alpha_{xx} = \alpha_{yy}$ ones in the $\mathrm{A_2}$ phase, and only the transverse $\alpha_{yx} = -\alpha_{xy}$ components in the $\mathrm{A_1}$ phase.

In the first part of Table VI, the spin-contributed longitudinal MECs are shown for $R\mathrm{MnO_3}$ and $\mathrm{LuFeO_3}$ in the $\mathrm{A_2}$ phase. The MEC from the spin channel is dominated by the spin-lattice contribution. Although the longitudinal magnetic charges of $\mathrm{LuFeO_3}$ are smaller than for $R\mathrm{MnO_3}$, the spin-lattice MECs $|\alpha_{zz}|$ in $R\mathrm{MnO_3}$ and $\mathrm{LuFeO_3}$ are similar, $\sim 0.25\,\mathrm{ps/m}$. The results are comparable to those reported for the transverse MEC in $\mathrm{Cr_2O_3}$[35] and for α_{zz} in $\mathrm{ErMnO_3}$[15] in previous first-principles calculations. In the second part of Table VI, we

TABLE V. Transverse magnetic charge components $Z^{\rm m}$ ($10^{-2}\mu_{\rm B}$/Å) of RMnO$_3$ and LuFeO$_3$ in the A$_2$ phase, as computed including or excluding SOC.

	HoMnO$_3$		ErMnO$_3$		YbMnO$_3$		LuMnO$_3$		LuFeO$_3$	
	Total	No SOC	Total	No SOC	Total	No SOC	Total	No SOC	Total	No SOC
$Z^{\rm m}_{xx}(\mathrm{R}_1)$	−23	−24	−21	−22	−37	−40	−42	−35	−36	−52
$Z^{\rm m}_{xx}(R_2)$	6	−1	6	3	12	9	14	6	15	24
$Z^{\rm m}_{yx}(R_2)$	16	18	11	12	10	10	8	7	−9	−11
$Z^{\rm m}_{xx}(\mathrm{TM})$	−2	10	−7	−10	−16	−21	−11	1	−52	−43
$Z^{\rm m}_{zx}(\mathrm{TM})$	−42	−24	−38	−22	−25	−34	−31	−17	−102	−95
$Z^{\rm m}_{yy}(\mathrm{TM})$	−5	46	−7	32	−22	27	−32	15	−16	−11
$Z^{\rm m}_{xx}(\mathrm{O}_{\rm T1})$	5	5	6	6	12	16	14	11	0	0
$Z^{\rm m}_{zx}(\mathrm{O}_{\rm T1})$	191	221	150	154	162	178	150	122	128	105
$Z^{\rm m}_{yy}(\mathrm{O}_{\rm T1})$	24	23	22	22	31	33	34	25	15	11
$Z^{\rm m}_{xx}(\mathrm{O}_{\rm T2})$	20	23	16	19	19	22	17	12	25	20
$Z^{\rm m}_{zx}(\mathrm{O}_{\rm T2})$	195	217	140	161	173	189	166	134	130	110
$Z^{\rm m}_{yy}(\mathrm{O}_{\rm T2})$	−59	−61	−48	−46	−57	−60	−57	−45	−41	−42
$Z^{\rm m}_{xx}(\mathrm{O}_{\rm P1})$	−445	−510	−392	−422	−532	−602	−564	−499	−665	−609
$Z^{\rm m}_{xx}(\mathrm{O}_{\rm P2})$	241	234	215	202	298	299	316	247	388	356
$Z^{\rm m}_{yx}(\mathrm{O}_{\rm P2})$	−378	−422	−335	−355	−466	−506	−498	−427	−673	−621

show the spin-related transverse MECs α_{xx} for RMnO$_3$ and LuFeO$_3$ in the A$_2$ phase. The same information is presented in graphical form in Fig. 4.

It is clear from the comparison between the first and second parts of Table VI that the transverse spin-lattice MECs are one order of magnitude larger than the longitudinal ones, as a result of the exchange-striction mechanism. Surprisingly, Fig. 4(a) shows that the effect of SOC on the exchange striction is profound, even reversing the sign of the spin-lattice MECs in RMnO$_3$. This unusual behavior can be traced mainly to two observations about the spin-lattice contributions from different IR-active modes in the RMnO$_3$ materials. Firstly, the exchange-striction MEC is smaller than expected as a result of a large degree of cancellation between the contributions from different transverse IR-active modes. To illustrate this, the mode-by-mode contributions are presented for a few selected cases in Table VII. Secondly, the softest modes are dominated by Mn displacements, precisely those for which SOC has the largest effect on the $Z^{\rm m}$ values, even flipping the sign of some components. In

TABLE VI. Computed MECs α_{zz} (longitudinal) and α_{xx} and α_{yx} (transverse) for RMnO$_3$ and LuFeO$_3$ (ps/m). Spin-lattice, spin-electronic, and total spin couplings are given as computed with and without SOC.

	Spin-latt.		Spin-elec.		Total spin	
	Total	No SOC	Total	No SOC	Total	No SOC
			α_{zz} in A$_2$ phase			
HoMnO$_3$	−0.27	0	0.06	0	−0.21	0
ErMnO$_3$	−0.26	0	0.05	0	−0.21	0
YbMnO$_3$	−0.25	0	0.06	0	−0.19	0
LuMnO$_3$	−0.19	0	0.00	0	−0.19	0
LuFeO$_3$	0.26	0	0.00	0	0.26	0
			α_{xx} in A$_2$ phase			
HoMnO$_3$	−0.99	5.12	4.10	4.83	3.11	9.95
ErMnO$_3$	−1.30	2.40	2.56	3.72	1.26	6.12
YbMnO$_3$	−2.52	1.20	3.72	4.66	1.20	5.86
LuMnO$_3$	−2.60	1.31	3.82	3.50	1.22	4.81
LuFeO$_3$	−2.20	−1.57	−0.79	−0.32	−2.99	−1.89
			α_{yx} in A$_1$ phase			
HoMnO$_3$	9.55	4.88	5.24	5.35	14.79	10.23

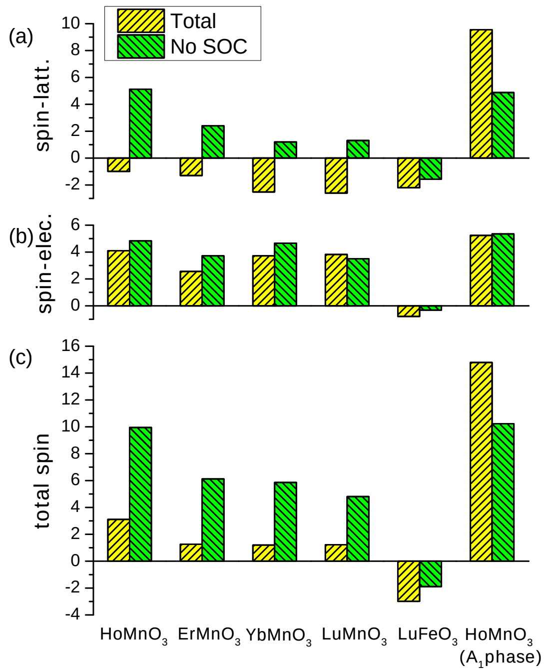

FIG. 4. Transverse MECs for RMnO$_3$ and LuFeO$_3$. α_{xx} (ps/m) in the A$_2$ phase and α_{yx} in the A$_1$ phase. (a) Spin-lattice; (b) spin-electronic; and (c) total spin couplings.

TABLE VII. Transverse MEC contributions (ps/m) from IR-active modes for A_2 and A_1 phases of $HoMnO_3$ and A_2 phase of $LuMnO_3$. Results are given in ascending order of force-constant eigenvalues, which are reported in Table II of the Supplement.

A_2 phase $HoMnO_3$		A_1 phase $HoMnO_3$		A_2 phase $LuFeO_3$	
Total	No SOC	Total	No SOC	Total	No SOC
0.01	0.12	0.25	0.18	0.28	0.39
−1.16	2.62	4.98	2.36	−0.54	−0.50
0.66	2.32	3.59	2.37	−1.31	−1.22
−0.51	−0.35	−0.32	−0.48	1.30	1.23
2.79	3.13	2.87	3.33	3.31	3.12
0.35	0.21	0.30	0.30	1.84	1.73
−1.88	−1.85	−1.35	−1.90	−4.43	−4.11
1.13	1.25	1.19	1.38	−2.59	−2.25
−2.96	−3.07	−2.70	−3.40	1.24	1.13
0.01	0.13	0.19	0.06	−1.48	−1.27
0.21	0.24	0.21	0.26	−0.15	−0.14
0.36	0.40	0.34	0.42	0.89	0.83
−0.03	−0.03	−0.03	−0.04	−0.62	−0.55
0.02	0.01	0.03	0.03	0.07	0.03

this way, it turns out that SOC can result in large relative changes in the MEC results. In the case of $LuFeO_3$, the SOC effect on the Z^{m} values is weak, even for Fe atoms. Thus, the MEC of $LuFeO_3$ does not change as dramatically as that of $R\mathrm{MnO}_3$ when SOC is included.

From Fig. 4(b) it can be seen that the spin-electronic contribution is not negligible in the transverse direction, and it counteracts the MEC from the spin-lattice channel in A_2 phase $R\mathrm{MnO}_3$. The total transverse ME effect is summarized in Fig. 4(c). Because of the large SOC effect and the cancellation between the lattice and electronic contributions, the total spin MEC α_{xx} is ~ 1.2 ps/m in most A_2-phase $R\mathrm{MnO}_3$ compounds, except for $HoMnO_3$. In $HoMnO_3$, the cancellation between the spin-lattice and the spin-electronic MECs is the weakest of all the $R\mathrm{MnO}_3$ compounds, resulting in the largest total spin MEC of ~ 3.1 ps/m in the A_2 phase. In $LuFeO_3$, the spin-lattice and spin-electronic terms are all smaller than in $R\mathrm{MnO}_3$. However, the cancellation induced by the SOC perturbation and the spin-electronic contribution is avoided, so that $LuFeO_3$ has a large total spin MEC of ~ -3 ps/m.

We present the MECs for $HoMnO_3$ in the A_1 phase in the last line of Table VI and in Fig. 4. In principle the MECs of $HoMnO_3$ in the A_1 and A_2 phases should be the same without SOC, as the two phases only differ by a global spin rotation. This is approximately confirmed by a comparison of the corresponding entries for $HoMnO_3$ in Table VI. The ME contribution from exchange striction (i.e., without SOC) is ~ 5 ps/m for both the A_2 and A_1 phases. However, when the effect of SOC is included, the spin-lattice contribution is strongly enhanced by another ~ 5 ps/m. Furthermore, the spin-electronic MEC has the same sign as the spin-lattice one, which adds ~ 5 ps/m to the MEC. Therefore, the total spin MEC α_{yx} reaches ~ 15 ps/m, and is the largest in all of the $R\mathrm{MnO}_3$ and $LuMnO_3$ materials we studied.

IV. SUMMARY

In summary, we have studied the spin-related magnetic charges and MECs for $HoMnO_3$, $ErMnO_3$, $YbMnO_3$, $LuMnO_3$, and $LuFeO_3$ using first-principles calculations. We confirm that the exchange striction acting on noncollinear spins induces much larger magnetic charges than does SOC acting alone. Nevertheless, the effect of SOC on the MECs is surprisingly large, rivaling that of exchange striction in many cases. This occurs because the exchange-striction contribution tends to be reduced by cancellations between different IR-active modes, while the SOC contribution is mainly associated with just a few low-frequency modes with large Mn displacements. We also find that the $R\mathrm{MnO}_3$ materials have spin-electronic MECs comparable to the spin-lattice ones. Among the $R\mathrm{MnO}_3$ and $LuFeO_3$ materials we studied, we find that the A_1 phase of $HoMnO_3$ is the most promising ME material, with the largest MEC of ~ 15 ps/m. Extrapolating our conclusions to other hexagonal $R\mathrm{MnO}_3$ and $R\mathrm{FeO}_3$ compounds that are not included in our calculations, we predict that the A_2 phase is more promising for the ferrites, while the A_1 phase has a stronger MEC for the manganites.

ACKNOWLEDGMENTS

We thank Weida Wu for useful discussions. The work was supported by ONR grant N00014-12-1-1035.

---

[*] mengye@physics.rutgers.edu
[1] M. Fiebig, J. Phys. D **38**, R123 (2005).
[2] N. A. Spaldin and M. Fiebig, Science **309**, 391 (2005).
[3] W. Eerenstein, N. D. Mathur and J. F. Scott, Nature **442**, 759 (2006).
[4] Y. Tokura, J. Magn. Magn. Mater. **310** 1145 (2007).
[5] S.-W. Cheong and M. Mostovoy, Nat. Mater. **6**, 13 (2007).
[6] R. Ramesh and N. A. Spaldin, Nat. Mater. **6**, 21 (2007).
[7] K. F. Wang, J.-M. Liu and Z. F. Ren, Adv. Phys. **58**, 321 (2009).
[8] M. Fiebig and N. A. Spaldin, Eur. Phys. J. B **71**, 293 (2009).
[9] J.-P. Rivera, Eur. Phys. J. B **71**, 299 (2009).
[10] D. Khomskii, Physics **2**, 20 (2009).
[11] T. Birol, N. A. Benedek, H. Das, A. L. Wysocki, A. T. Mulder, B. M. Abbett, E. H. Smith, S. Ghosh, and C. J.

Fennie, Curr. Opin. Solid State Mater. Sci. **16**, 227 (2012).

[12] E. Bousquet, N. A. Spaldin, and K. T. Delaney, Phys. Rev. Lett. **106**, 107202 (2011).

[13] J. Íñiguez, Phys. Rev. Lett. **101**, 117201 (2008).

[14] K. T. Delaney, M. Mostovoy and N. A. Spaldin, Phys. Rev. Lett **102**, 157203 (2009).

[15] H. Das, A. L. Wysocki, Y. Geng, W. Wu and C. J. Fennie, Nat. Commun. **5**, 2998 (2014).

[16] M. Ye and D. Vanderbilt, Phys. Rev. B **89**, 064301 (2014).

[17] M. Mostovoy, Nat. Mater. **9**, 188 (2010).

[18] B. B. Van Aken, T. T. M. Palstra, A. Filippetti and N. A. Spaldin, Nat. Mater. **3**, 164 (2004).

[19] C. J. Fennie and K. M. Rabe, Phys. Rev. B **72**, 100103 (2005).

[20] Y. Kumagai and N. A. Spaldin, Nat. Commun. **4**, 1540 (2013).

[21] S. Artyukhin, K. T. Delaney, N. A. Spaldin and M. Mostovoy, Nat. Mater. **13**, 42 (2013).

[22] T. Choi, Y. Horibe, H. T. Yi, Y. J. Choi, W. Wu and S.-W. Cheong, Nat. Mater. **9**, 253 (2010).

[23] S.-Z. Lin, X. Wang, Y. Kamiya, G.-W. Chern, F. Fan, D. Fan, B. Casas, Y. Liu, V. Kiryukhin, W. H. Zurek, C. D. Batista and S.-W. Cheong, Nature Phys. **10**, 970 (2014).

[24] M. Fiebig, Th. Lottermoser and R. V. Pisarev, J. Appl. Phys. **93**, 8194 (2003).

[25] F. Yen, C. D. Cruz, B. Lorenz, E. Galstyan, Y. Y. Sun, J. Mater. Res. **22**, 2163 (2007).

[26] B. Lorenz, ISRN Condens. Matter Phys. **2013**, 43 (2013).

[27] Y. Geng, H. Das, A. L. Wysocki, X. Wang, S-W. Cheong, M. Mostovoy, C. J. Fennie and W. Wu, Nat. Mater. **13**, 163 (2014).

[28] W. Wang, J. Zhao, W. Wang, Z. Gai, N. Balke, M. Chi, H. N. Lee, W. Tian, L. Zhu, X. Cheng, D. J. Keavney, J. Yi, T. Z. Ward, P. C. Snijders, H. M. Christen, W. Wu, J. Shen and X. Xu, Phys. Rev. Lett. **110**, 237601 (2013).

[29] S. M. Disseler, J. A. Borchers, C. M. Brooks, J. A. Mundy, J. A. Moyer, D. A. Hillsberry, E. L. Thies, D. A. Tenne, J. Heron, J. D. Clarkson, G. M. Stiehl, P. Schiffer, D. A. Muller, D. G. Schlom, W. D. Ratcliff, arXiv:1411.1694 (2014).

[30] G. Kresse and J. Furthmüller, Phys. Rev. B **54**, 11169 (1996).

[31] J. P. Perdew, K. Burke, and M. Ernzerhof, Phys. Rev. Lett. **77**, 3865 (1996).

[32] P. E. Blochl, Phys. Rev. B **50**, 17953(1994); G. Kresse and D. Joubert, Phys. Rev. B **59**, 1758 (1999).

[33] A. I. Liechtenstein, V. I. Anisimov, and J. Zaanen, Phys. Rev. B **52**, R5467 (1995)

[34] R. D. King-Smith and D. Vanderbilt, Phys. Rev. B **47**, 1651 (1993).

[35] A. Malashevich, S. Coh, I. Souza and D. Vanderbilt, Phys. Rev. B **86**, 094430 (2012).